GPS Solutions (2024) 28:179
https://doi.org/10.1007/s10291-024-01727-2

ORIGINAL ARTICLE

Long-term analysis of NRTK positioning performances over one solar activity cycle from 2013 to 2023

Jinsheng Zhang[1,2] · Xiaodong Ren[1] · Dengkui Mei[1] · Ahmed Abdelaziz[1] · Xiaohong Zhang[1,3] · Guofu Pan[2] · Ke Jiang[2]

Received: 11 April 2024 / Accepted: 6 August 2024

Abstract
As the 25th solar cycle is approaching its peak, the Real-time Kinematic (RTK) positioning performance is significantly affected by solar activity and the ionosphere. This study focuses on a triangulation network in the Hong Kong region with baseline lengths ranging from 10 to 20 km. The rover station is located at a distance of 16 km from the nearest reference station. A complete dataset spanning the entire solar activity cycle from 2013 to 2023 was collected for analysis. Virtual observations of the rover station's position were generated using Network RTK (NRTK) processing mode. The results show that during years of low solar activity, the overall fixing rate exceeds 80%. However, in years of high solar activity, the fixing rate exhibits a noticeable correlation with local time, reaching its lowest point at around 16:00 local time, dropping to approximately 66%. In years of low solar activity, the horizontal and vertical accuracy, with a 95% confidence level, remain below 5 cm and 10 cm, respectively. In contrast, during years of high solar activity, the accuracy deteriorates to 7.5 cm and 13 cm in the horizontal and vertical direction. In addition, as the Vertical Total Electron Content (VTEC) increases, the RTK positioning performance gradually declines. On the other hand, with the increase of Rate of TEC Index (ROTI), the RTK positioning performance deteriorates rapidly.

Keywords Real-time kinematic · Total electron content (TEC) · Rate of TEC index (ROTI) · Solar activity · Fixing rate

Introduction

The ionosphere is a region in the Earth's atmosphere typically ranging from about 50 to 1000 km above the Earth's surface, primarily caused by the radiation of high-energy ultraviolet and X-rays from the sun (Pereira et al. 2021; Aa et al. 2023). When electromagnetic wave signals traverse from the upper atmosphere to the Earth's surface, they are subject to the influence of the ionosphere (Yeh et al. 1982; Aarons. 1982; Klobuchar. 1987; Koucká et al. 2021). Presently, the ionosphere stands as a prominent error source in the domain of high-precision Global Navigation Satellite System (GNSS) navigation and positioning. Ionospheric scintillation phenomena have significant impacts on the performance of GNSS, leading to rapid changes in signal phase and amplitude and affecting positioning accuracy and reliability (Dierendonck et al. 1993; Kim et al. 2014; Juan et al. 2017; Moraes et al. 2018; Liu et al. 2023).

Real-time kinematic (RTK) positioning is widely used in surveying and mapping, monitoring, navigation, and other aspects due to its advantages of simple algorithms, fast convergence, high positioning accuracy, and reliability. However, in some cases, such as the active ionospheric conditions, the RTK positioning performance faces a serious challenge because the atmospheric delay error cannot be eliminated by the difference of measurements.

Tominaga et al. (2004) evaluated the relationship between mesoscale baseline (around 46 km) ionospheric errors and carrier phase positioning errors. They found that ambiguity resolution was difficult for the mesoscale baseline during some periods. Under active ionospheric conditions or ionospheric storms, it is difficult for NRTK users to reach a fixed solution (Luo et al. 2005; Wielgosz et al. 2005; Gianniou et al. 2012; Dobelis et al. 2017; Paziewski et al. 2022). Especially in low latitude areas, when the distance between

✉ Xiaodong Ren
xdren@whu.edu.cn

1 School of Geodesy and Geomatics, Wuhan University, Wuhan 430079, Hubei, China

2 Guangzhou Hi-Target Navigation Tech Co.Ltd., Guangzhou 511400, Guangdong, China

3 Chinese Antarctic Center of Surveying and Mapping, Wuhan University, Wuhan 430079, Hubei, China

reference stations exceeds 30 km, the terminal positioning performance will significantly decrease (Charoenkalunyuta et al. 2012). Pluta (2013) and Follestad et al. (2021) analyzed the impact of the ionosphere on GPS-RTK positioning accuracy which was related to seasonality and local time. Bae et al. (2018) analyzed the performance of the ionosphere on NRTK navigation applications. In dynamic mode, even low-cost devices connected to high-quality GNSS antennas could achieve comparable accuracy and stability as surveying-grade devices. Odolinski et al. (2019) evaluated the positioning performance of smartphone and low-cost multi-system single- and dual-frequency RTK during periods of low, medium, and high ionospheric disturbances. They found that at a baseline length of 8.9 km, both sets of devices could achieve instantaneous ambiguity resolution when the Kp index reached 3o. Additionally, during calm ionospheric periods, they compared the positioning performance of a 21.8 km baseline. Dutta et al. (2022) predicted that there would be several occurrences of cycle slips on multiple satellites during the worst months, leading to RTK float solutions or DGNSS.

It can be seen that the influence of the ionosphere on high-precision positioning performance has been widely concerned and some research results and progress have been obtained. However, these studies mainly focus on the analysis of positioning performance under specific geomagnetic storm events, or assess the impact of ionosphere on the precision positioning performance within a short period of time, such as several tens of days, and some of them are dominated by PPP positioning (Psychas et al. 2019; Su et al. 2019; Lu et al. 2020; Li et al. 2023b; Lyu et al. 2023).

Considering that the new solar activity cycle will reach the active peak around 2025 (Okoh et al. 2018), it is not known whether and to what extent the ionospheric activity under the new solar activity cycle will affect RTK and other precision positioning technologies. Through this study, we aim to gain a clearer understanding of the NRTK positioning accuracy and ambiguity fixing rate during low and high ionospheric activity. Further, we investigate the key factors causing this degradation in RTK positioning performance. Additionally, we aim to identify the optimal time of day for achieving the desired RTK positioning accuracy, thus providing guidance for field engineering surveys.

Therefore, this paper quantitatively analyzes the positioning accuracy and fixing rate of RTK positioning for a whole solar cycle of 11 years. The relationships between Vertical Total Electron Content (VTEC), Rate of TEC Index (ROTI) and positioning performances of RTK are analyzed during the high and low solar activity years in one solar cycle. Since low-latitude regions are prone to ionospheric anomalies, this study mainly focuses on analyzing the effects of the ionosphere on positioning performance in low-latitude areas, especially in China.

Data and methodology

This section begins by providing an overview of the source of the experimental data, followed by an introduction to the RTK positioning method. Finally, a detailed description is presented regarding the data processing strategies utilized in this study.

Data

This study is conducted within the geographical area of Hong Kong, bounded by longitude 114° E to 114.5° E and latitude 22.15° N to 22.55° N. The study utilizes four reference stations, namely HKKT, HKOH, HKST, and HKWS as illustrated in Fig. 1 (https://rinex.geodetic.gov.hk/). The observational datasets cover an entire solar activity cycle, spanning from January 1, 2013, to December 31, 2023. Due to the large volume of data and computational constraints, a systematic sub-sampling approach is employed. This approach involves extracting a set of sample data every 7 days, ensuring both the precision and reliability of the data analysis while managing the computational load effectively.

The NRTK method requires at least 3 reference stations to provide VRS correction messages. Hence, we have statistically analyzed the data completeness rate of three reference stations over the 11 years (2013–2023). In this paper, we follow a pattern of selecting 1 day every 7 days, resulting in a total of 52 days per year. We consider the data to be valid when all three stations have data simultaneously. The statistical results are shown in the following Table 1.

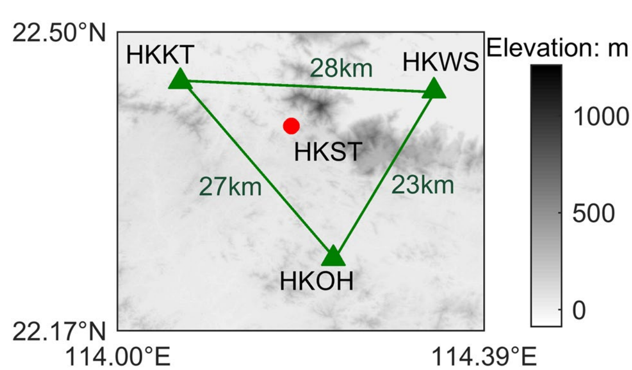

Fig. 1 Schematic representation of the triangulation network in the Hong Kong region. Triangular points represent reference stations, and the red dot denotes rover station. The rover station is located at a distance of 16 km from the nearest reference station

Table 1 data completeness rate of three reference stations with simultaneous data over the past 11 years (2013–2023)

Year	Available days
2013	52
2014	52
2015	52
2016	52
2017	51
2018	52
2019	52
2020	51
2021	52
2022	52
2023	52

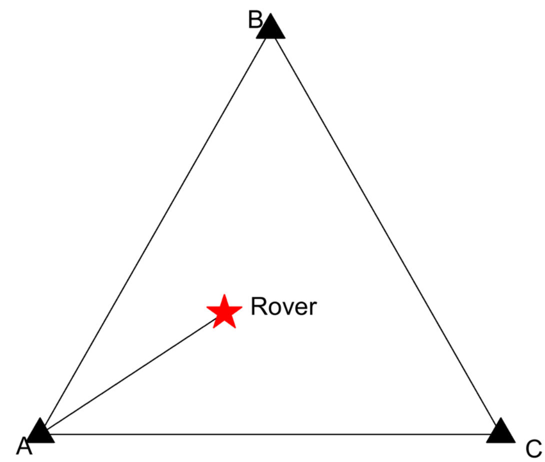

Fig. 2 The schematic diagram of a triangulation network

Methods

NRTK method

The observation equations associated with pseudorange and carrier phase are defined as Ren et al. (2020):

$$\begin{cases} P^{i}_{k,j} = \rho^{i}_{0,j} + d^{i}_{ion,k,j} + d^{i}_{trop,j} + c\left(\tau^{i} - \tau_{j}\right) + d^{i}_{k} + d_{k,j} + \varepsilon^{i}_{p,k,j} \\ L^{i}_{k,j} = \rho^{i}_{0,j} - d^{i}_{ion,k,j} + d^{i}_{trop,j} + c\left(\tau^{i} - \tau_{j}\right) - \lambda N^{i}_{k} + d^{i}_{k} + d_{k,j} + \varepsilon^{i}_{L,k,j} \end{cases} \tag{1}$$

where i is the satellite; j is the receiver; k denotes frequency;ρ is the satellite-to-receiver range; P represents the pseudorange observation; L represents the carrier phase observation; d_{ion} stands for ionospheric delay error; d_{trop} is the tropospheric delay error; τ_j denotes the receiver clock error; τ^i is the satellite clock error; d represents the differential code bias between the satellite and the receiver; N^i_k represents the initial integer ambiguity;ε_p and ε_L represent the measurement errors of pseudorange and phase respectively and their variances can be modeled as a simplified function of the elevation angle (Dai et al. 2017):

$$\sigma^2 = a^2 + b/\sin^2\theta \tag{2}$$

where θ is the elevation angle of the satellite, a and b can be set empirically.

The baseline solution of Continuously Operating Reference Stations (CORS) typically employs a double-difference mode, where the coordinates of the reference stations at both ends of the baseline are obtained in advance, thus serving as known values during the solution process. Without loss of generality, the observation equation for the double-differenced baseline can be expressed as follows:

$$\begin{cases} \Delta\nabla P^{ij}_{k,rb} = \Delta\nabla\rho^{ij}_{k,rb} + \Delta\nabla I^{ij}_{k,rb} + \Delta\nabla T^{ij}_{k,rb} + \Delta\nabla\varepsilon^{ij}_{P_{k,rb}} \\ \Delta\nabla L^{ij}_{k,rb} = \Delta\nabla\rho^{ij}_{k,rb} - \Delta\nabla I^{ij}_{k,rb} + \Delta\nabla T^{ij}_{k,rb} - \lambda\Delta\nabla N^{ij}_{k,rb} + \Delta\nabla\varepsilon^{ij}_{L_{k,rb}} \end{cases} \tag{3}$$

where $\Delta\nabla$ represents the double-difference between stations and satellites. The parameters to be estimated include $\Delta\nabla d_{trop}$, $\Delta\nabla d_{ion,k}$, and $\Delta\nabla N_k$. Since the ambiguities possess integer characteristics after double differencing, it is necessary to fix the double-difference integer ambiguities in order to obtain high-precision information on double-difference tropospheric and ionospheric information (Teunissen. 1995; Gao et al. 2002; Odijk et al. 2010; Platz. 2023).

The baseline network is configured with reference stations HKKT, HKOH, and HKWS, forming a triangulation network, while HKST serves as the designated rover station, as illustrated in Fig. 1. Utilizing the same procedure, the double-difference tropospheric and ionospheric information for the three baselines of the triangle is separately calculated (Vollath et al. 2002; Chen et al. 2003; Dai et al. 2003). Following the interpolation principle within the triangle, tropospheric and ionospheric model values at the interior of the triangle's rover station positions can be interpolated. Subsequently, by adjusting these values to the nearest reference station observations, virtual observations of the rover station positions can be obtained. Figure 2 illustrates a schematic diagram of a triangulation network, where A, B, and C are reference stations. According to the ionospheric information of baselines AB and AC, the following system of equations can be formulated:

$$\begin{bmatrix} \Delta E_{AB} & \Delta N_{AB} \\ \Delta E_{AC} & \Delta N_{AC} \end{bmatrix} \begin{bmatrix} \alpha \\ \beta \end{bmatrix} = \begin{bmatrix} \Delta\nabla d_{ion,AB} \\ \Delta\nabla d_{ion,AC} \end{bmatrix} \tag{4}$$

where ΔE represents coordinate difference in the east direction between stations; ΔN represents coordinate difference in the north direction between stations; $\Delta\nabla d_{ion,AB}$ and $\Delta\nabla d_{ion,AC}$ respectively indicate the ionospheric data derived from the calculations of baseline AB and AC; α and β represent interpolation coefficients, which can be obtained through least squares calculation based on (4). The ionospheric interpolation at the rover station is as follows:

$$\Delta\nabla \mathrm{d}_{\mathrm{ion,Rover}} = \alpha\Delta \mathrm{E}_{\mathrm{AR}} + \beta\Delta \mathrm{N}_{\mathrm{AR}} \tag{5}$$

RTK method

In this study, the NRTK mode was used to generate virtual reference stations that are very close to the rover station (within a few tens of meters). Consequently, after double differencing between the base and satellite stations, the errors caused by the ionosphere and troposphere can largely cancel each other out. Therefore, (3) can be simplified to the form of (6):

$$\begin{cases} \Delta\nabla \mathrm{P}_{\mathrm{k,rb}}^{\mathrm{ij}} = \Delta\nabla\rho_{\mathrm{k,rb}}^{\mathrm{ij}} + \Delta\nabla\varepsilon_{\mathrm{pk,rb}}^{\mathrm{ij}} \\ \Delta\nabla \mathrm{L}_{\mathrm{k,rb}}^{\mathrm{ij}} = \Delta\nabla\rho_{\mathrm{k,rb}}^{\mathrm{ij}} - \lambda\Delta\nabla \mathrm{N}_{\mathrm{k,rb}}^{\mathrm{ij}} + \Delta\nabla\varepsilon_{\mathrm{Lk,rb}}^{\mathrm{ij}} \end{cases} \tag{6}$$

Assuming there are $m + 1$ common-view satellites between the reference station and the rover station, the double-difference observation equation from (6) can be written in matrix form as follows:

$$\mathbf{Y} = \begin{bmatrix} \mathbf{Y_P} \\ \mathbf{Y_L} \end{bmatrix} \tag{7}$$

where $\mathbf{Y_P} = \left[\Delta\nabla P_{1,rb}^{i1}, \Delta\nabla P_{2,rb}^{i1}, .., \Delta\nabla P_{1,rb}^{im}, \Delta\nabla P_{2,rb}^{im}\right]^{\mathrm{T}}$, $\mathrm{Y_L} = \left[\Delta\nabla L_{1,rb}^{i1}, \Delta\nabla L_{2,rb}^{i1}, \ldots, \Delta\nabla L_{1,rb}^{im}, \Delta\nabla L_{2,rb}^{im}\right]^{\mathrm{T}}$. Therefore, the parameters to be estimated are as follows:

$$\begin{aligned} \mathbf{X} &= \left[\mathbf{X_{pos}}, \mathbf{X_{amb}}\right]^{\mathbf{T}} \\ &= \left[\mathbf{x_{rb}}, \mathbf{y_{rb}}, \mathbf{z_{rb}}, \Delta\nabla\mathbf{N_{1,rb}^1}, \Delta\nabla\mathbf{N_{2,rb}^1}, \ldots, \Delta\nabla\mathbf{N_{1,rb}^m}, \Delta\nabla\mathbf{N_{2,rb}^m}\right]^{\mathbf{T}} \end{aligned} \tag{8}$$

The random model of the observations after double differencing is given by (9):

$$\mathrm{D} = \begin{bmatrix} \mathrm{TD_{SD}^P T^T} & \\ & \mathrm{TD_{SD}^L T^T} \end{bmatrix} \tag{9}$$

where the matrix T is the transformation matrix from single difference to double difference, with the column having a value of -1 representing the reference satellite:

$$\mathbf{T} = \begin{bmatrix} 1 & & & -1 & & \\ 1 & & & -1 & & \\ & 1 & & -1 & & \\ & 1 & & -1 & & \\ & & \cdots & \vdots & \cdots & \\ & & & -1 & 1 & \\ & & & -1 & 1 & \\ & & & -1 & & 1 \\ & & & -1 & & 1 \end{bmatrix}_{2(\mathrm{m}-1),2\mathrm{m}} \tag{10}$$

The variance–covariance matrices of pseudorange and phase single-difference observations are given by (11) and (12) respectively, where σ^2 represents the variance of the original non-differenced observations from (2):

$$\mathbf{D_{SD}^P} = \begin{bmatrix} \left(\sigma_{1,r}^{1,P}\right)^2 + \left(\sigma_{1,b}^{1,P}\right)^2 & & & & \\ & \left(\sigma_{2,r}^{1,P}\right)^2 + \left(\sigma_{2,b}^{1,P}\right)^2 & & & \\ & & \ddots & & \\ & & & \left(\sigma_{1,r}^{m,P}\right)^2 + \left(\sigma_{1,b}^{m,P}\right)^2 & \\ & & & & \left(\sigma_{2,r}^{m,P}\right)^2 + \left(\sigma_{2,b}^{m,P}\right)^2 \end{bmatrix}_{2\mathrm{m},2\mathrm{m}} \tag{11}$$

$$\mathbf{D_{SD}^L} = \begin{bmatrix} \left(\sigma_{1,r}^{1,L}\right)^2 + \left(\sigma_{1,b}^{1,L}\right)^2 & & & & \\ & \left(\sigma_{2,r}^{1,L}\right)^2 + \left(\sigma_{2,b}^{1,L}\right)^2 & & & \\ & & \ddots & & \\ & & & \left(\sigma_{1,r}^{m,L}\right)^2 + \left(\sigma_{1,b}^{m,L}\right)^2 & \\ & & & & \left(\sigma_{2,r}^{m,L}\right)^2 + \left(\sigma_{2,b}^{m,L}\right)^2 \end{bmatrix}_{2\mathrm{m},2\mathrm{m}} \tag{12}$$

In dynamic GPS navigation positioning, a discretized Kalman filtering model is often employed, with the linearized equations as follows:

$$\begin{cases} \overline{\mathbf{X}}_k = \mathbf{\Phi}_{k,k-1}\hat{\mathbf{X}}_{k-1} \\ \mathbf{V}_k = \mathbf{A}_k\hat{\mathbf{X}}_k - \mathbf{Y}_k \end{cases} \tag{13}$$

where $\overline{\mathbf{X}}_k$ is the predicted state vector at time t_k; $\hat{\mathbf{X}}_k$ and $\hat{\mathbf{X}}_{k-1}$ are the estimated values at times t_k and t_{k-1} respectively; $\mathbf{\Phi}_{k,k-1}$ denotes the state transition matrix; $\mathbf{A}_k$ denotes the observation design matrix; $\mathbf{Y}_k$ represents the double-difference observation vector at time t_k. The covariance matrix of $\overline{\mathbf{X}}_k$ is given by the following equation:

$$\mathbf{\Sigma}_{\overline{X}_k} = \mathbf{\Phi}_{k,k-1}\mathbf{\Sigma}_{\hat{X}_{k-1}}\mathbf{\Phi}^{T}_{k,k-1} + \mathbf{\Sigma}_{W_k} \tag{14}$$

where $\mathbf{\Sigma}_{\hat{X}_{k-1}}$ is variance of the estimated value at t_{k-1}, and $\mathbf{\Sigma}_{W_k}$ represents the process noise. In contrast to high-dynamic scenarios involving aircraft, vehicles and similar movements, most situations encountered during NRTK user operations exhibit low-dynamic walking modes. Furthermore, considering a data sampling interval of 5 s in this study, only position parametrs ($\mathbf{X}_{\mathbf{pos}}$ in eqution (8)) are taken into account during state prediction, omitting velocity and acceleration parameters (Takasu et al. 2009). The specific form is shown in (15):

$$\begin{cases} \overline{\mathbf{X}}_{k(pos)} = \hat{\mathbf{X}}_{k(spp)} \\ \overline{\mathbf{X}}_{k(amb)} = \hat{\mathbf{X}}_{k-1(amb)} \end{cases} \tag{15}$$

where $\hat{\mathbf{X}}_{k(spp)}$ denotes the estimated parameters of single-point positioning coordinates at time t_k, $\hat{\mathbf{X}}_{k-1(amb)}$ represents the filtered estimates of ambiguity parameters at time t_{k-1}. and the covariance of $\overline{\mathbf{X}}_k$ is expressed by (16):

$$\mathbf{\Sigma}_{\overline{X}_k} = \begin{bmatrix} \mathbf{\Sigma}_{\hat{X}_{k(spp)}} & \\ & \mathbf{\Sigma}_{\hat{X}_{k-1(amb)}} \end{bmatrix}_{2m+3,2m+3} \tag{16}$$

where the $\mathbf{\Sigma}_{\hat{X}_{k(spp)}}$ represents the variance matrix of single-point positioning coordinates parameters at time t_k, and the value of each diagonal element is 100 m^2 in this study; $\mathbf{\Sigma}_{\hat{X}_{k-1(amb)}}$ denotes the variance matrix of the filtered estimates of ambiguity parameters at time t_{k-1}. Subsequently, Kalman filtering measurement updates are conducted by integrating dynamic models with actual measurement data of t_k.

TEC extraction

Considering the simplicity and effectiveness of the single-layer model in describing electron content in the ionosphere, this study has chosen the single-layer model for ionospheric analysis. Ionospheric VTEC serves as a metric quantifying the quantity of electrons passing through a unit area, denominated in Total Electron Content Unit (TECU). By leveraging dual-frequency observational data and employing the carrier phase smoothing pseudorange method, the Slant Total Electronic Content (STEC) along the slant propagation path is calculated (Liu et al. 2020; Li et al. 2023a, 2024).

$$\begin{cases} P_4 = P^i_{1,j} - P^i_{2,j} = 40.28\left(\frac{1}{f_1^2} - \frac{1}{f_2^2}\right)STEC + c\left(B^i + B_j\right) \\ L_4 = L^i_{1,j} - L^i_{2,j} = 40.28\left(\frac{1}{f_2^2} - \frac{1}{f_1^2}\right)STEC + c\left(B^i + B_j\right) - \left(\lambda_1 N_1 - \lambda_2 N_2\right) \end{cases} \tag{17}$$

where P_4 represents the pseudorange observation without geometric distance; c is the speed of light; $B^i = d^i_1 - d^i_2$ stands for Differential Code Bias (DCB) of the satellite, corrected in this study using the DCB product released by the Chinese Academy of Sciences (Wang et al. 2016; Zhang et al. 2019); $B_j = d_{1,j} - d_{2,j}$ is the differential code bias of the receiver. To enhance the accuracy of P_4, a Hatch filter is applied for carrier phase smoothing pseudorange (Abdelazeem et al. 2016; Mazher et al. 2016). For continuous observation arcs, the smoothing method is defined as follows:

$$\begin{cases} P4_{sm}(t) = \frac{k-1}{k}\left[P4_{sm}(t-1) + L_4(t) - L_4(t-1)\right] + \frac{1}{k}P_4(t),\ t > 1 \\ P4_{sm}(1) = P_4(1) = 1,\ t = 1 \end{cases} \tag{18}$$

where $P4_{sm}$ represents the smoothed pseudorange observation; t denotes epoch; k is the total number of epochs from the start of smoothing. Substituting into (17), we obtain:

$$STEC = \frac{f_1^2 f_2^2}{40.28\left(f_2^2 - f_1^2\right)} \cdot \left[P4_{sm} - c\left(B^i + B_j\right)\right] \tag{19}$$

The STEC is ultimately transformed into the VTEC above the measurement station using a single-layer model projection function. The process is as follows:

$$VTEC = \cos\left(\arcsin\left(\frac{R}{R+H}\sin(\alpha z)\right)\right) \cdot STEC \tag{20}$$

where z represents the elevation angle of the satellite; R is the radius of the Earth; H is the height of the mapping function, specifically the height where the electron density peaks, with a chosen value of 506.7 km in this study; α is a constant, equal to 0.9782 (Schaer. 1999; Xiang et al. 2019).

ROTI index

In addition to calculating ionospheric VTEC, this paper also computes the ROTI index to analyze variations in the fixing rate and accuracy of RTK under perturbed conditions. By calculating the temporal rate of ionospheric STEC (ROT) over a specific duration, this provides information on ionospheric disturbances (Pi et al. 1997; Zhao et al. 2022):

$$\mathrm{ROT} = \frac{\mathrm{STEC}(\mathrm{t}+\triangle\mathrm{t}) - \mathrm{STEC}(\mathrm{t})}{\triangle\mathrm{t}} \tag{21}$$

where $\triangle t$ represents the temporal variation of ionospheric STEC. The ROTI can be calculated as follows:

$$\mathrm{ROTI} = \sqrt{\langle \mathrm{ROT}^2 \rangle - \langle \mathrm{ROT} \rangle^2} \tag{22}$$

where $\langle\rangle$ represents the average value over a time interval.

In this study, we use a 30-s data sampling for ROT calculations and a 5-min time interval for ROTI calculations.

Data process strategies

NRTK strategies

The NRTK technology improves the positioning accuracy of rover stations by utilizing data from multiple reference stations (Vollath et al. 2002; Chen et al. 2003; Dai et al. 2003). More GPS data processing details refer to Table 2.

Fixing rate

Least-squares AMBiguity Decorrelation Adjustment (LAMBDA) is an algorithm used to resolve carrier phase ambiguities (Teunissen. 1995). The "ratio" evaluation metric is commonly used to determine the reliability of the ambiguity resolution. Specifically, this ratio is calculated by comparing the ambiguity residuals of the optimal solution and the second-best solution (Teunissen et al. 2004). In the context of this study, a fixed solution requires the satisfaction of the following requirements simultaneously:(a) The ambiguity search and fixing are conducted using the LAMBDA method, with a ratio threshold of 2.0. The definition of the "ratio" mentioned can be referenced from this particular literature; (b) The error between the positioning result of the rover station in the horizontal direction and the true value is less than 10 cm; (c) The error between the positioning result of the rover station in the vertical direction and the true value is less than 20 cm; (d) Epochs during the filter convergence process are excluded.

Results and discussions

In this section, we will analyze the changes in RTK positioning performances in low-latitude regions throughout the solar activity cycle. We will also examine the effects of diurnal variations in the ionosphere on RTK positioning. Additionally, we will analyze the impact of ionospheric parameters such as VTEC and ROTI on RTK positioning and reasons of RTK performance degradation throughout the solar activity cycle.

Table 2 Correction models and estimation strategies for GPS NRTK positiong

Items	Descriptions	
	Server side	User side
GNSS system	GPS	
GNSS signals	L1, L2	
Data sampling interval	5 s	
A priori noise	Pseudorange: 0.3 m; carrier-phase: 0.003 m	
Combination mode	Double difference L4 (ionosphere-free combination)	Double difference L1&L2
Elevation mask	10°	
Minimum number of satellite	4	
Estimator	Sequential least squares	Kalman filter
Weight of obervation	Elevation-dependent weight	
Phase ambiguties	WL-L1 cascade fixing with Constants for each continuous observation arc	L1&L2 partial fixing with Constants for each continuous observation arc
Receiver coordinate	Fixed	Estimated in the epoch-wise kinematic model with a priori noise of 10 m
Ionospheric delays	First order eliminate, higher order ignore	Corrected by linear interpolation model (LIM)
Tropospheric delays	Dry Component: Modeled by Sasstamoinen with Neil Mapping Function (NMF) (Neil. 1996) Wet Componet: Hourly constants with process noise of 1 cm/$\sqrt{h}$ and NMF	Corrected by linear interpolation model (LIM)

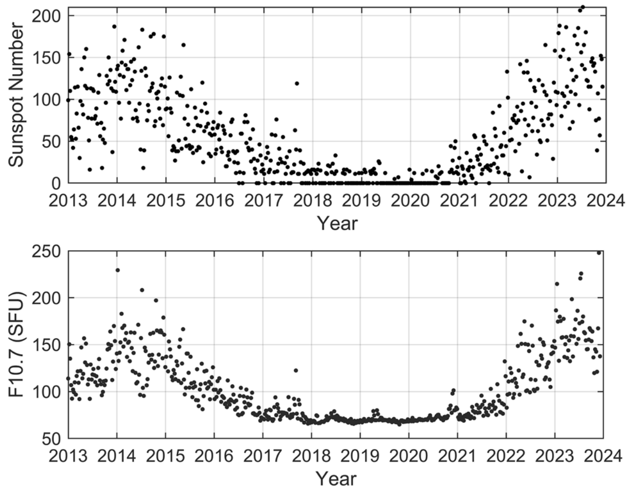

Fig. 3 Daily variations of Sunspot Number and F10.7 indices from 2013 to 2023

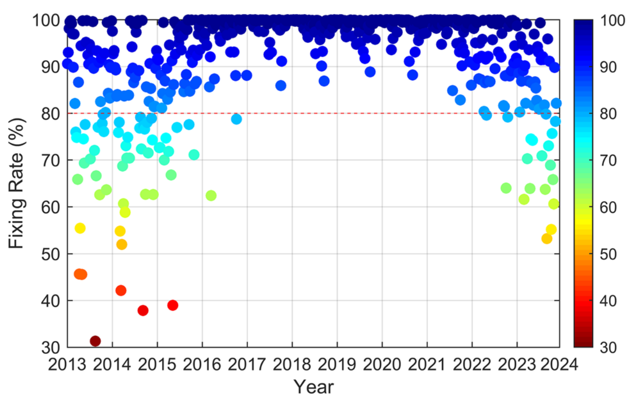

Fig. 4 Time series of RTK positioning fixing rate from 2013 to 2023

Solar activity analysis

Figure 3 illustrates the day-to-day fluctuations in sunspot number and F10.7 indices from 2013 to 2023, and the data can be accessed from https://omniweb.gsfc.nasa.gov/form/dx1.html. The sunspot number is widely employed to gauge the intensity and periodicity of solar activity, reflecting its cyclical variations. The F10.7 index is measured in solar flux units (SFU) and reflects the strength of solar radio flux. According to Chinese meteorological standards (https://www.sws.bom.gov.au/Educational/1/2/4), solar activity levels can be classified as follows: values below 80 SFU indicate low solar activity, 80 SFU to 150 SFU represent moderate solar activity, and values exceeding 150 SFU indicate high solar activity. Periods in which the F10.7 index exceed 100 SFU are classified as high solar activity years (from 2013 to 2015 and from 2022 to 2023), while those falling below this threshold correspond to low solar activity years (from 2016 to 2021).

Relation with solar activity

Figure 4 depicts the variation in fixing rates for the rover stations from 2013 to 2023. The red dashed line in the figure represents the caution line, commonly considered in engineering practice, indicating that fixing rates below 80% are generally considered unreliable for providing high-precision positioning services. It is observable from Fig. 4 that during years of high solar activity, fixing rates frequently fall below 80%. Conversely, in years of low solar activity, the fixing rates remain above 80%. The overall trend aligns with the solar activity variations observed throughout the entire solar activity cycle in Fig. 3, suggesting a significant periodic influence of solar activity on the fixing rates of RTK.

Table 3 presents the percentage of fixing solution accuracy in the horizontal and vertical directions for rover stations during the period from 2013 to 2023. It should be noted that when assessing the accuracy of the results, the reference coordinates (HKST station) are the precise coordinates provided by the Hong Kong Geodetic Survey official website. (https://www.geodetic.gov.hk/common/data/

Table 3 Statistical results of fixing solution accuracy percentage in the horizontal and vertical directions from 2013 to 2023

Year	Percentage in the horizontal direction (%)			Percentage in the vertical direction (%)		
	Ɛ < 2 cm	2 < Ɛ < 5 cm	Ɛ > 5 cm	Ɛ < 5 cm	5 < Ɛ < 10 cm	Ɛ > 10 cm
2013	72.49	20.12	7.39	86.33	9.32	4.35
2014	69.08	22.13	8.79	85.18	10.55	4.27
2015	77.11	17.40	5.50	88.74	8.43	2.83
2016	85.87	12.33	1.79	92.62	6.01	1.37
2017	88.28	10.36	1.37	94.60	4.53	0.87
2018	90.16	8.48	1.36	94.99	4.17	0.84
2019	89.37	9.20	1.42	94.59	4.50	0.91
2020	89.66	9.19	1.15	94.98	4.22	0.80
2021	84.68	13.30	2.02	92.74	5.84	1.42
2022	75.49	19.88	4.63	86.96	9.17	3.87
2023	62.27	28.79	8.94	78.93	13.36	7.71

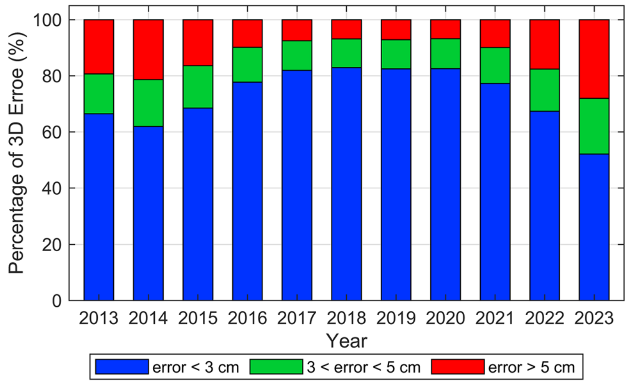

Fig. 5 Three-dimensional error percentage from 2013 to 2023

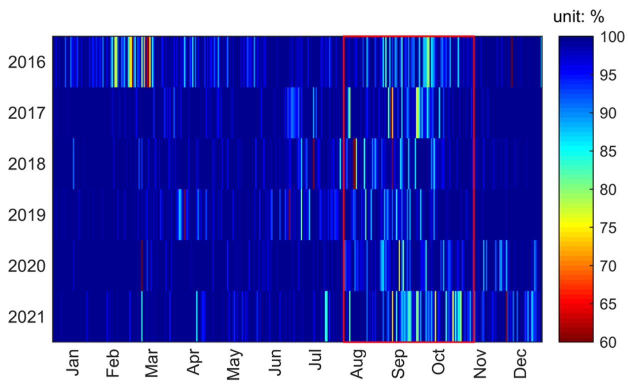

Fig. 6 Heat map of fixing rates for the HKST station from 2016 to 2021. The vertical axis represents the years, while the horizontal axis represents the day of the year. The color gradient from red to blue signifies an increasing fixing rate (color figure online)

pdf/SatRef_Coord.pdf). The years of high solar activity are 2013, 2014, 2015, 2022, and 2023. Additionally, the Three-dimensional (3D) error percentage chart are shown in Fig. 5. From Fig. 5, it can be observed that the proportion of 3D errors below 3 cm at the HKST station during high solar activity years is significantly lower compared to low solar activity years. Conversely, the proportion of errors exceeding 5 cm is noticeably higher during high solar activity years than during low solar activity years. Detailed precision numerical features in horizontal and vertical direction can be found in Table 3.

Furthermore, the fixing rates of the rover station in Fig. 4 exhibit noticeable periodic fluctuations, despite being derived from datasets with a 7-days interval. To mitigate potential randomness in the results and minimize the impact of solar activity interference, a reanalysis was performed using daily datasets from periods of low solar activity, as depicted in Fig. 6. The graph reveals a decline in fixing rates during the autumn season, as highlighted within the red-boxed region. During the autumnal equinox, when the Sun

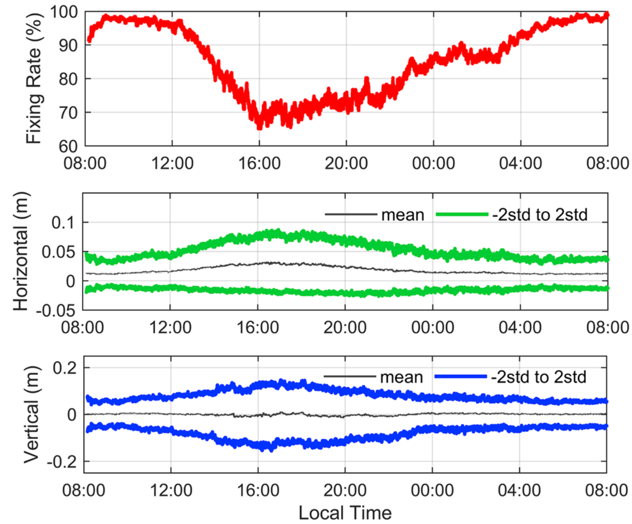

Fig. 7 Variation of fixing rate and precision with local time in high solar activity years. The top panel illustrates the fixing rate, the middle and bottom panel depict the horizontal and vertical precision within 95% confidence interval

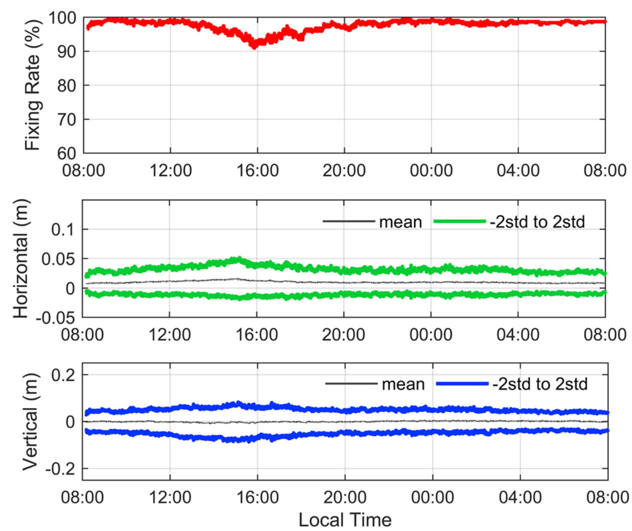

Fig. 8 Variation of fixing rate and precision with local time in low solar activity years. The top panel illustrates the fixing rate, the middle and bottom panel depict the horizontal and vertical precision within the 95% confidence interval

is directly over the Earth's equator, increased ionospheric activity often occurs in low-latitude regions. Fluctuations in electron density within the ionosphere can cause signal attenuation, multipath propagation, and phase variations, thereby affecting the reception and processing of GNSS signals. Sanz et al. (2014) noted in their study of ionospheric activity indicators that ionospheric activity in low-latitude regions exhibits significant seasonal dependence.

Taking into account the diurnal variation of the ionosphere at the same location caused by the Earth's rotation, this study further classifies all results based on local time. The average fixing rates and fixing precision at each moment during high and low years of solar activity are calculated, as shown in Fig. 7 and Fig. 8.

From Fig. 7, it can be observed that during years of high solar activity, the fixing rate is consistently above 90% from 08:00 Local Time (LT) to 12:00 LT. During this time period, the horizontal and vertical error are within 5 cm and 10 cm, respectively. Starting from 12:00 LT, the fixing rate and precision begin to decrease, reaching the lowest values around 16:00 LT, with a fixing rate of only 66%. At this time, the horizontal and vertical direction errors at a 95% confidence level reach 7.5 cm and 13 cm, respectively, no longer meeting the requirement for centimeter-level high-precision services. From 16:00 LT to 00:00 LT, the fixing rate and precision gradually improve but remain at a lower level. This is likely due to the fact that as the sun approaches the horizon, solar radiation must pass through a thicker atmospheric layer to reach the ground, causing changes in electron density and distribution in the ionosphere (Moreno et al. 2011; Gao et al. 2023). After 00:00 LT, the fixing rate and precision gradually return to normal levels.

From Fig. 8, it is evident that during years of low solar activity, the fixing rate remains consistently above 90% throughout the day. The horizontal and vertical accuracy, at a 95% confidence level, is consistently better than 5 cm and 10 cm, respectively. Only minor fluctuations are observed at 16:00 LT, indicating overall stable and reliable performances.

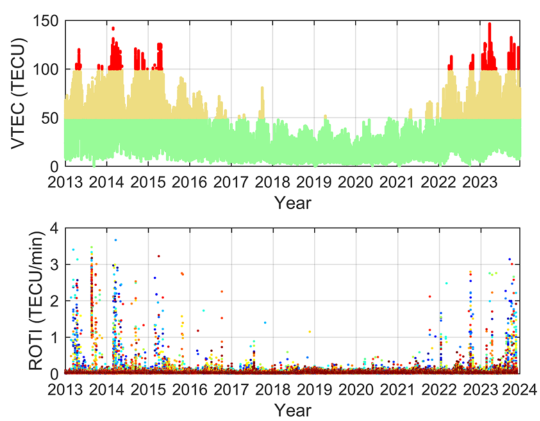

Fig. 9 Variations of VTEC and ROTI from 2013 to 2023. The top panel illustrates the VTEC from the HKST station. The bottom panel depicts the ROTI from the HKST station, with a temporal resolution of 5 min. Both data sampling of VTEC and ROTI are 30 s

Relation with ionospheric indices

The time series of the VTEC and ROTI values from 2013 to 2023 are shown in Fig. 9. It can be observed that during periods of low solar activity, the VTEC generally peaks around 40 TECU, occasionally exceeding 60 TECU. In contrast, during years of high solar activity, the VTEC peaks surpass 120 TECU, approximately three times the values observed during low years of solar activity. According to Pereira et al. (2021), a ROTI value exceeding 0.2 TECU/min indicates the occurrence of ionospheric irregularities. The analysis

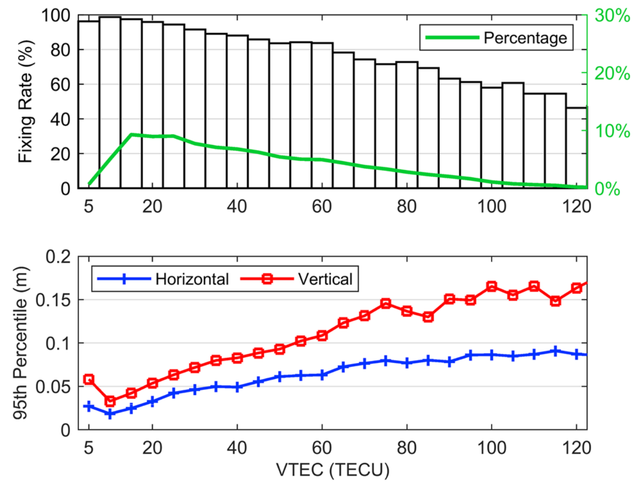

Fig. 10 Variation in RTK positioning results during years of high solar activity with respect to VTEC. The top panel represents the fixing rate, with green line indicating the percentage of VTEC in each interval. The bottom panel illustrates the 95% confidence level for horizontal and vertical accuracy

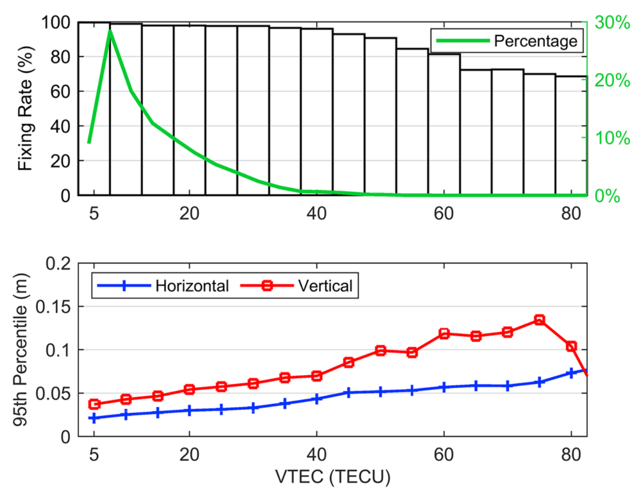

Fig. 11 Variation in RTK positioning results during years of low solar activity with respect to VTEC. The top panel represents the fixing rate, with green line indicating the percentage of VTEC in each interval. The bottom panel illustrates the 95% confidence level for horizontal and vertical accuracy

of Fig. 9 reveals that during low years of solar activity, the majority of ROTI values remain below 0.2 TECU/min, suggesting overall ionospheric stability. However, in high years of solar activity, numerous instances exhibit ROTI values exceeding 0.2 TECU/min, indicating frequent occurrences of ionospheric disturbances.

To analyze the variations in RTK fixing rate and accuracy concerning VTEC, this study grouped VTEC values in increments of 5 TECU and examined the corresponding changes in positioning results. The results for high and low years of solar activity are illustrated in Fig. 10 and Fig. 11, respectively. It is evident from Fig. 10 to Fig. 11 that as VTEC values increase, the fixing rate exhibits a decreasing trend. Particularly when VTEC values exceed approximately 60 TECU, the fixing rate falls below 80%, with horizontal directional errors exceeding 5 cm at a 95% confidence level, while the vertical directional errors surpassing 10 cm. Statistical analysis revealed that during years of high solar activity, the proportion of ionospheric VTEC values exceeding 60 TECU is 23.1%, with the majority occurring in the afternoon. In contrast, during low solar activity years, this proportion is only 0.73%. This suggests that during years of high solar activity, the ionospheric VTEC values exert a greater influence on the fixing rate of RTK, especially in the afternoon.

To analyze the variations in fixing rate and accuracy under ionospheric irregular disturbances, this study considers the maximum satellite ROTI value within each epoch as the ROTI for that epoch. The ROTI values from all epochs are then grouped into intervals for analysis. Intervals within 0.2 TECU/min are categorized with an interval size of 0.02, intervals above 0.2 TECU/min are

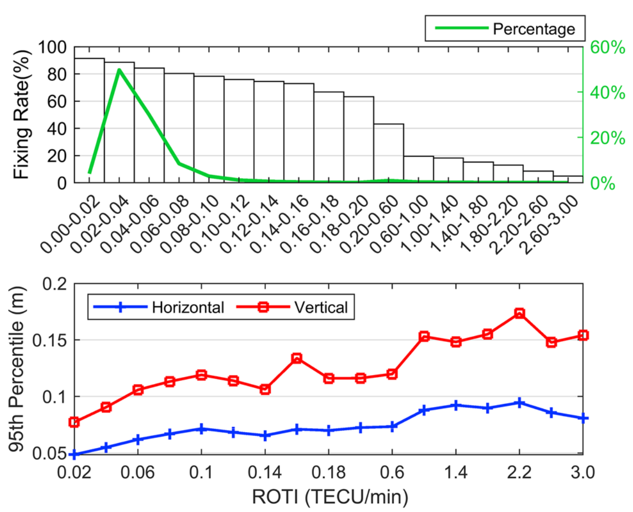

Fig. 12 Variation in RTK positioning results during years of high solar activity with respect to ROTI. The top panel represents the fixing rate, while the bottom panel depicts the 95% confidence level in horizontal and vertical accuracy

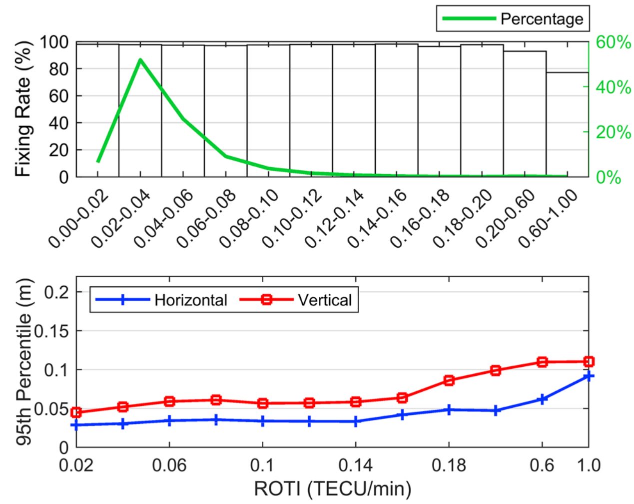

Fig. 13 Variation in RTK positioning results during years of low solar activity with respect to ROTI. The top panel represents the fixing rate, while the bottom panel depicts the 95% confidence level in horizontal and vertical accuracy

categorized with an interval size of 0.4. The results for years of high solar activity and low solar activity are presented separately in Fig. 12 and Fig. 13.

Figure 12 reveals that during years of high solar activity, when the ROTI value reaches approximately 0.08 TECU/min, the fixing rate begins to drop below 80%. As the ROTI value continues to increase, both fixing rate and accuracy exhibit a sharp decline, falling significantly below the standards for high-precision services.

As can be seen from Fig. 13, during the low solar activity years, when the ROTI value is between 0.6 and 1.0, the fixing rate is slightly below 80%. In contrast, as shown in Fig. 12, during the high solar activity years, when the ROTI value is between 0.6 and 1.0, the fixing rate has dropped rapidly below 20%.

RTK performance degradation analysis

To analyze the reasons for the deterioration of positioning accuracy, we conducted an in-depth analysis focusing on the number of cycle slips and the interpolation accuracy of the ionosphere.

We selected 10 days of data from both high solar activity years and low solar activity years. Cycle slip detection was performed using the TurboEdit method (Blewitt. 1990). For analyzing the ionospheric interpolation accuracy of a rover station, we use the method of treating the rover station as a reference station for baseline calculation and compute the double-difference ionospheric values which were considered as the true values. Then the 68th percentile error and the 95th percentile error were statistically analyzed.The results are shown in the Table 4 below.

Table 4 Statistics of Cycle Slips and Ionospheric Interpolation Accuracy for 10 Days in High and Low Solar Activity Years

Date		Fixing rate (%)	Cycle slip		Ionospheric interpolation accuracy	
			Number of cycle slip	Total number of satellites	68th percentile error (cm)	95th percentile error (cm)
High solar activity days	2013/4/9	45.7	4035	146939	1.25	7.76
	2013/4/16	55.5	3236	147772	1.16	9.61
	2014/3/12	42.2	5430	146429	1.02	7.44
	2014/9/10	37.9	1875	146913	1.65	11.22
	2015/4/23	66.8	580	152890	0.93	3.00
	2015/5/7	39.0	1118	152944	0.96	5.15
	2022/10/1	64.0	2397	153900	1.30	12.54
	2023/2/19	61.6	761	153971	1.36	7.15
	2023/3/19	63.7	1356	153457	0.93	3.39
	2023/8/27	53.2	874	148137	1.41	13.36
Low solar activity days	2016/1/1	99.9	12	155866	0.60	1.28
	2016/6/17	99.7	22	156545	0.71	2.01
	2017/1/1	99.8	14	156411	0.57	1.25
	2017/6/11	99.8	27	156759	0.69	2.03
	2018/1/1	99.9	24	156628	0.57	1.24
	2018/6/18	99.9	33	154365	0.66	1.54
	2019/1/1	99.8	34	154846	0.57	1.22
	2019/6/19	99.6	6	153909	0.77	2.70
	2020/1/1	99.9	13	150592	0.56	1.23
	2021/1/1	99.9	15	153502	0.56	1.27

Column 4 of Table 4 represents the number of cycle slips detected at the rover station (HKST). Comparing the 10-days cycle slip results during high solar activity years with those during low solar activity years, it is evident that the frequency of cycle slips in high solar activity years is approximately 10 to 100 times higher than in low solar activity years. Due to the frequent occurrence of cycle slips, the number of satellites available for RTK positioning is greatly reduced, resulting in a significant decrease in the overall fixing rate.

Columns 6 and 7 of the Table 4 represent the ionospheric interpolation accuracy of the NRTK server at 68% and 95% confidence levels, respectively. This value characterizes the accuracy of the generated VRS observations. During the 10 days of low solar activity, the ionospheric interpolation errors are all less than 1 cm at 68% confidence level and less than 3 cm at 95% confidence level. However, during the 10 days of high solar activity, most of the ionospheric interpolation errors are greater than 1 cm at 68% confidence level, and many exceed 5 cm or even 10 cm at 95% confidence level. As the ionospheric interpolation error of the NRTK server increases, indicating poorer VRS observation accuracy, it deviates more from the assumption of (6) (that the double-differenced ionosphere between short baselines can be neglected). As seen in (6), when the double-differenced ionospheric residuals between VRS observations and rover observations are larger, the impact on the ambiguity parameters and coordinate parameters is greater, resulting in a lower RTK fixing rate.

Conclusions

This paper investigates the RTK positioning performances in low-latitude Hong Kong region during different solar activity levels within one solar cycle. Specifically, this paper thoroughly analyzes the relationship between the fixing rate and fixing accuracy with the VTEC and ROTI. The conclusions as follows:

(1) Trends in ambiguity fixing rates and accuracy from 2013 to 2023 are generally consistent with solar activity levels. In addition, fixing rates also exhibit seasonal cyclical characteristics.

(2) In high solar activity years, there is a strong correlation between the fixing rate and local time. Particularly around 16:00 LT, the fixing rate reaches its lowest point, dropping to 66%. It's important to note that the

specific time periods of significant impact may vary depending on the region.

(3) When VTEC reaches 60 TECU, RTK positioning performance may not meet the requirement. In high solar activity years, 23.1% of VTEC exceed 60 TECU. In the lower years, this proportion was only 0.73%. When ROTI reach approximately 0.08 TECU/min in high solar activity years or around 0.2 TECU/min in low solar activity years, the ionospheric disturbance impedes the achievement of stable centimeter-level high-precision positioning services in the vertical direction.

(4) There are two main reasons for RTK positioning performance declines. Firstly, the frequency of cycle slips increase significantly during high solar years, which is up to 10 times or even more compared to low solar activity years. Secondly, during high solar activity years, the accuracy of ionospheric interpolation values declines, and many of them can reach 5 cm or even 10 cm at a 95% confidence level.

Acknowledgements The authors are grateful for the use of GPS observation data provided by Hong Kong Geodetic Survey services (https://rinex.geodetic.gov.hk/rinex2/). This research was funded by the National Natural Science Foundation of China (No.42230104, No.42174031), the Fundamental Research Funds for the Central Universities, and the Knowledge Innovation Program of Wuhan-Shuguang. The numerical calculations have been done on the supercomputing system in the Supercomputing Center of Wuhan University.

Author contributions JSZ, XDR and XHZ conceived and defined the research theme. JSZ processed of the data and wrote the manuscript. GFP and XDR discussed the methodological feasibility and provided data analysis. KJ carried out image process work. XHZ, DKM and AA revised the entire manuscript. All authors reviewed the manuscript.

Funding National Natural Science Foundation of China,No.42230104,No.42174031,No.42230104,No.42174031,No.42230104,No.42174031,No.42230104,No.42174031,No.42230104,No.42174031

Data availability F10.7 and sunspot data from National Aeronautics and Space Administration (NASA, via https://omniweb.gsfc.nasa.gov/form/dx1.html); Observation data from Hong Kong Geodetic Survey services (https://rinex.geodetic.gov.hk/rinex2/).

Declarations

Conflict of interest The authors declare no competing interests.

References

Aa E, Zhang SR, Erickson PJ, Wang WB, Qian LY, Cai XG, Coster AJ, Goncharenko LP (2023) Significant Mid- and Low-Latitude Ionospheric Disturbances Characterized by Dynamic EIA, EPBs, and SED Variations During the 13–14 March 2022 Geomagnetic Storm. J Geophy Res: Space Phy. https://doi.org/10.1029/2023JA031375

Aarons J (1982) Global morphology of ionospheric scintillations. Proc IEEE 70(4):360–378. https://doi.org/10.1109/PROC.1982.12314

Abdelazeem M, Celik RN, Rabbany AE (2016) Comparative study of GPS-TEC smoothing techniques. Acta Geod Geophys 51:659–670. https://doi.org/10.1007/s40328-015-0153-1

Bae TS, Kim M (2018) Performance Analysis of Network-RTK Techniques for Drone Navigation considering Ionospheric Conditions. J Sensors 1:5154697. https://doi.org/10.1155/2018/5154697

Blewitt G (1990) An automatic editing algorithm for GPS data. Geophys Res Lett 17(3):199–202

Charoenkalunyuta T, Satirapod C, Lee HK (2012) Choi YS (2012) Performance of network-based RTK GPS in low-latitude region: A case study in Thailand. Eng J 16(5):95–104. https://doi.org/10.4186/ej.2012.16.5.95

Chen XM, Landau H, Vollath U (2003) New Tools for Network RTK Integrity Monitoring. In: Proceedings ION GPS 2003, Institute of Navigation, Portland, Oregon, USA, September 9–12, pp 1355–1360

Dai LW, Han SW, Wang JL, Rizos C (2003) Comparison of interpolation algorithms in network-based GPS techniques. Navigation 50(4):277–293. https://doi.org/10.1002/j.2161-4296.2003.tb00335.x

Dai W, Shi Q, Cai C (2017) Characteristics of the BDS Carrier Phase Multipath and Its Mitigation Methods in Relative Positioning. Sensors 17(4):796

Dierendonck JV, Klobuchar AJ, Hua Q (1993) Ionospheric scintillation monitoring using commercial single frequency C/A code receivers. In: Proceedings of ION GPS 1993, Institute of Navigation, Salt Lake City, Utah, USA, pp 1333–1342

Dobelis D, Zvirgzds J, Kaļinka M (2017) High ionospheric activity effects on LatPos RTK network performance in Latvia. In: IOP Conf Ser: Mater Sci Eng, IOP Publish 251(1):012064. https://doi.org/10.1088/1757-899X/251/1/012064

Dutta U, Jarlemark P, Rieck C, Johansson J (2022) Ionospheric Effects on GNSS RTK. In: Proceedings of the 35th International Technical Meeting of the Satellite Division of The Institute of Navigation (ION GNSS+ 2022): pp.1589–1598.

Follestad A, Clausen L, Moen JI, Jacobsen KS (2021) Latitudinal, diur-nal, and seasonal variations in the accuracy of an RTK positioningsystem and its relationship with ionospheric irregularities. SpaceWeather 19(6):e2020SW002625. https://doi.org/10.1029/2020SW002625

Gao XW, Liu JN, Ge MR (2002) An ambiguity searching method for network RTK baselines between base stations at single epoch. Acta Geod Et Cartogr Sinica 31(4):305–309. https://doi.org/10.3321/j.issn:1001-1595.2002.04.005

Gao HY, Zhang DH, Liu ZZ, Sun SJ, Hao YQ, Xiao Z (2023) Revisiting the Variation of the Ionospheric Irregularities in the Low Latitude Region of China Based on Small Regional Geodetic GNSS Station Network. Sp Weather. https://doi.org/10.1029/2023SW003452

Gianniou M, Mitropoulou E (2012) Impact of high ionospheric activity on GPS surveying: Experiences from the Hellenic RTK-network during 2011–12. EUREF Annual Symp 2012:6–8

Juan JM, Angel AA, Sanz J, Casado GG, Garcia AR (2017) A method for scintillation characterization using geodetic receivers operating at 1 Hz. J Geod 91(11):1383–1397. https://doi.org/10.1007/s00190-017-1031-0

Kim M, Seo J, Lee J (2014) A Comprehensive Method for GNSS Data Quality Determination to Improve Ionospheric Data Analysis. Sensors 14(8):14971–14993. https://doi.org/10.3390/s140814971

Klobuchar JA (1987) Ionospheric time-delay algorithm for single-frequency GPS users. IEEE Trans Aerosp Electron Syst 23(3):325–331. https://doi.org/10.1109/TAES.1987.310829

Koucká Knížová P, Laštovička J, Kouba D, Mošna Z, Podolská K, Potužníková K, Šindelářová T, Chum J, Rusz J (2021) Ionosphere infuenced from lower-lying atmospheric regions. Front Astron Sace Sci 8:651445. https://doi.org/10.3389/fspas.2021.651445

Li W, Wang K, Yuan K (2023a) Performance and Consistency of Final Global Ionospheric Maps from Different IGS Analysis Centers. Remote Sensing 15(4):1010. https://doi.org/10.3390/rs15041010

Li XX, Han JJ, Li X, Huang JX, Shen ZH, Wu ZZ (2023b) A grid-based ionospheric weighted method for PPP-RTK with diverse network scales and ionospheric activity levels. GPS Solut. https://doi.org/10.1007/s10291-023-01522-5

Li M, Zha JP, Yuan YB, Liu T, Zhang X, Zhao CB (2024) A unified model of multi-GNSS and multi-frequency precise point positioning for the joint estimation of ionospheric TEC and time-varying receiver code bias. J Geod. https://doi.org/10.1007/s00190-023-01808-z

Liu T, Zhang B, Yuan Y, Zhang X (2020) On the application of the raw-observation-based PPP to global ionosphere VTEC modeling: an advantage demonstration in the multi-frequency and multi GNSS context. J Geod 94(1):1. https://doi.org/10.1007/s00190-019-01332-z

Liu H, Ren XD, Zhang XH, Mei DK, Yang PX (2023) Investigating the Effects of Ionospheric Scintillation on Multi-Frequency BDS-2/BDS-3 Signals at Low Latitudes. Sp Weather. https://doi.org/10.1029/2022SW003362

Lu YW, Wang ZJ, Ji SY, Chen W (2020) Assessing the positioning performance under the effects of strong ionospheric anomalies with multi-GNSS in Hong Kong. Radio Sci. https://doi.org/10.1029/2019RS007004

Luo N, Dao TD, Lachapelle G, Cannon E(2005) GPS Network RTK Performance Under Very Active Ionospheric Conditions. In: Proceedings of the 18th International Technical Meeting of the Satellite Division of The Institute of Navigation (ION GNSS 2005), Long Beach, CA, USA, September 13–16, pp 2531–2539.

Lyu S, Xiang Y, Tang T, Pei L, Yu W, Truong TK (2023) A Consistent Regional Vertical Ionospheric Model and Application in PPP–RTK Under Sparse Networks. Journal of the Institute of Navigation. https://doi.org/10.33012/navi.568

Mazher K, Tahir M, Ali K (2016) GNSS pseudorange smoothing: Linear vs non-linear filtering paradigm. IEEE Aerosp Conf, Big Sky, MT, USA 2016:1–10. https://doi.org/10.1109/AERO.2016.7500779

Moraes AO, Vani BC, Costa E, Abdu MA, Paula ER, Sousasantos J, Monico JFG, Forte B, Negreti PMS, Shimabukuro MH (2018) GPS availability and positioning issues when the signal paths are aligned with ionospheric plasma bubbles. GPS Solut 22(4):1–12. https://doi.org/10.1007/s10291-018-0760-8

Moreno B, Radicella S, Lacy MC, Herraiz M, Caderot GR (2011) On the efects of the ionospheric disturbances on precise point positioning at equatorial latitudes. GPS Solut 15:381–390. https://doi.org/10.1007/s10291-010-0197-1

Odijk D, Teunissen PJG (2010) Improving the speed of CORS Network RTK ambiguity resolution. Position Locat Navig Symp (PLANS), IEEEI ON. https://doi.org/10.1109/PLANS.2010.5507203

Odolinski R, Teunissen PJG (2019) An assessment of smartphoneand low-cost multi-GNSS single-frequency RTK positioning forlow, medium and high ionospheric disturbance periods. J Geod 93(5):701–722. https://doi.org/10.1007/s00190-018-1192-5

Okoh DI, Seemala GK, Rabiu AB, Uwamahoro J, Habarulema JB, Aggarwal M (2018) A Hybrid Regression-Neural Network (HR-NN) method for forecasting the solar activity. Sp Weather 16:1424–1436. https://doi.org/10.1029/2018SW001907

Paziewski J, Høeg P, Sieradzki R, Jin Y, Jarmolowski W, Hoque MM, Berdermann J, Hernandez-PajaresM WP, Lyu H, Miloch WJ, Perez O (2022) Theimplications of ionospheric disturbances for precise GNSS posi-tioning in Greenland. J Space Weather Space Clim 12:33. https://doi.org/10.1051/swsc/2022029

Pereira VAS, Monico JFG (2021) Camargo PO (2021) Detection of solar flare using IGS network stations: case study for September 6. Rev Bras Geom 9(2):103–119. https://doi.org/10.3895/rbgeo.v9n2.13418

Pi X, Mannucci AJ, Lindqwister UJ, Ho CM (1997) Monitoring of global ionospheric irregularities using the worldwide GPS network. Geophys Res Lett 24(18):2283–2286. https://doi.org/10.1029/97GL02273

Platz HD (2023) On the equivalence of ionospheric-free, differenced, and undifferenced uncombined GNSS network processing. GPS Solut. https://doi.org/10.1007/s10291-023-01510-9

Pluta M (2013) (2013) The influence of condition of the ionosphere on the accuracy of Real Time Kinematic GPS measurements. Geomat Environ Eng 7(2):59–69. https://doi.org/10.7494/geom.2013.7.2.59

Psychas D, Verhagen S, Liu X, Memarzadeh Y, Visser H (2019) Assessment of ionospheric corrections for PPP-RTK using regional ionosphere modelling. Meas Sci Technol 30(1):014001. https://doi.org/10.1088/1361-6501/aaefe5

Ren XD, Chen J, Li XX, Zhang XH (2020) Ionospheric total electron content estimation using GNSS carrier phase observations based on zero-diference integer ambiguity: methodology and assessment. IEEE Trans Geosci Remote Sens 59(1):817–830. https://doi.org/10.1109/TGRS.2020.2989131

Sanz J, Juan JM, González-Casado G, Prieto-Cerdeira R, Schlueter S, Orús R (2014) Novel ionospheric activity indicator specificallytailored for GNSS users. In: Proceedings ION GNSS 2014, Institute of Navigation, Tampa, Florida, USA, September 8–12, p 1173–1182

Schaer S (1999) Mapping and predicting the Earth's ionosphere usingthe Global Positioning System. Geod-Geophys Arb Schweiz, 59.

Su K, Jin SG, Hoque M (2019) Evaluation of Ionospheric delay effects on Multi-GNSS positioning performance. Remote Sens 11(2):171. https://doi.org/10.3390/rs11020171

Takasu T, Yasuda A (2009) Development of the low-cost RTKGPS receiver with an open source program package RTKLIB. In: International Symposium on GPS/GNSS, International Convention Center Jeju, Korea, Nov 4–6

Teunissen PJG (1995) The least-squares ambiguity decorrelation adjustment: a method for fast GPS integer ambiguity estimation. J Geod 70(1–2):65–82. https://doi.org/10.1007/BF00863419

Teunissen PJG, Verhagen S (2004) On the foundation of the popularratio test for GNSS ambiguity resolution. In: Proc. ION GNSS2004, Institute of Navigation, Long Beach, California, USA, Sep-tember 21–24, pp 2529–2540

Tominaga T, Kondo K, Kubo N, Yasuda A(2004) The Ionospheric Effect on Medium Baseline RTK-GPS Positioning. In: The 2004 International Symposium on GNSS/GPS, Sydney, Australia

Vollath U, Landau H, Chen XM, Doucet K, Pagels C (2002) Network RTK versus single base RTK-understanding the error characteristics. In: Proceedings ION GPS 2002, Institute of Navigation, Portland, Oregon, USA, September 24–27, pp 2774–2781

Wang NB, Yuan YB, Li ZS, Montenbruck O, Tan BF (2016) Determination of differential code biases with multi-GNSS observations. J Geod 90:209–228. https://doi.org/10.1007/s00190-015-0867-4

Wielgosz P, Kashani I, Grejner-Brzezinska D (2005) Analysis of long-range network RTK during a severe ionospheric storm. J Geodesy 79(9):524–531. https://doi.org/10.1007/s00190-005-0003-y
Xiang Y, Gao Y (2019) An Enhanced Mapping Function with Ionospheric Varying Height. Remote Sensing 11(12):1497
Yeh KC, Liu CH (1982) Radio wave scintillations in the ionosphere. Proc IEEE 70(4):324–360. https://doi.org/10.1109/PROC.1982.12313
Zhang B, Teunissen PJG, Yuan Y, Zhang X, Li M (2019) A modified carrier-to-code leveling method for retrieving ionospheric observables and detecting short-term temporal variability of receiver differential code biases. J Geod 93(1):19–28. https://doi.org/10.1007/s00190-018-1135-1
Zhao D, Li W, Li C, Hancock CM, Roberts GW, Wang Q (2022) Analysis on the ionospheric scintillation monitoring performance of ROTI extracted from GNSS observations in high-latitude regions. Adv Space Res 69(1):142–158. https://doi.org/10.1016/j.asr.2021.09.026

Jinsheng Zhang received B. Sc. and master's degrees in geodesy and engineering surveying from Central South University in 2011 and 2014respectively. Currently, he is pursuing the Ph.D. degree with Wuhan University, Wuhan, China. He focuses on network RTK and ionospheric modelling.

Xiaodong Ren is an associate professor at Wuhan University. He obtained his B.Sc., Master, and Ph.D. degrees with distinction in Geodesy and Engineering Surveying at the School of Geodesy and Geomatics in Wuhan University in 2011, 2013, and 2017. His main research focuses on PPP-RTK and ionospheric modeling.

Dengkui Mei received B. Sc. and master's degrees in geodesy and engineering surveying from Changsha University of Science & Technology in 2017 and 2020, respectively. Currently, he is pursuing the Ph.D. degree with Wuhan University, Wuhan, China. He focuses on ionospheric remote sensing and ionospheric impacts on GNSS precise positioning.

Ahmed Abdelaziz is PhD student at Wuhan University, teaching assistant at Benha University, Egypt. He obtained his B.Sc. degree in civil engineering from Benha University, his master degree in GNSS from Beihang university, Beijing, China. His main research focuses on PPP, convergence time and ionosphere modelling.

Xiaohong Zhang is currently a professor at Wuhan University. He obtained his B.Sc., Master, and Ph.D. degrees with distinction in Geodesy and Engineering Surveying at the School of Geodesy and Geomatics in Wuhan University in 1997, 1999, and 2002. His main research interests include Precise Point Positioning and GNSS/INS.

Guofu Pan is a professor level senior engineer at Guangzhou Hi-Target Navigation Tech Co.Ltd.. He obtained his B.Sc. and master's in Geodesy and Engineering Surveying at the School of Geodesy and Geomatics in Wuhan University in 2007 and 2012. His main research focuses on GNSS/INS navigation.

Ke Jiang is a GNSS R&D engineer at Guangzhou Hi-Target Navigation Tech Co.Ltd.. She obtained her B.Sc. and master's in School of Geography and Information Engineering at China University of Geosciences in 2019 and 2022. Her main research focuses on PPP-RTK and ionosphere modelling.